Journal of Geophysical Research: Atmospheres

RESEARCH ARTICLE
10.1029/2017JD027977

Key Points:

- The QBO modulates the amplitude and the spatial distribution of the MJO-related North Pacific storm track (NPST) change
- Baroclinic energy conversion and downstream energy propagation dominate the dynamical processes of the NPST change
- The QBO-MJO-NPST relationship is partly explained by the differences in the MJO amplitude and its associated circulation

Correspondence to:
H.-M. Kim,
hyemi.kim@stonybrook.edu

Citation:
Wang, J., Kim, H.-M., Chang, E. K. M., & Son, S.-W. (2018). Modulation of the MJO and North Pacific storm track relationship by the QBO. *Journal of Geophysical Research: Atmospheres*, *123*. https://doi.org/10.1029/2017JD027977

Received 27 OCT 2017
Accepted 2 APR 2018
Accepted article online 9 APR 2018

Modulation of the MJO and North Pacific Storm Track Relationship by the QBO

Jiabao Wang[1], Hye-Mi Kim[1], Edmund K. M. Chang[1], and Seok-Woo Son[2]

[1]School of Marine and Atmospheric Sciences, Stony Brook University, Stony Brook, NY, USA, [2]School of Earth and Environmental Sciences, Seoul National University, Seoul, South Korea

Abstract This study demonstrates a possible impact of the quasi-biennial oscillation (QBO) on the Madden-Julian Oscillation (MJO)-related North Pacific storm track (NPST) change during October–March for the period of 1979–2016. The NPST shows significant intraseasonal changes in response to the MJO. In general, when the MJO convection is located over the Indian Ocean (western to central Pacific), the NPST tends to shift poleward (southward). This MJO-related NPST change has larger amplitude during the easterly phase of the QBO (EQBO) than during its westerly phase (WQBO). The spatial distribution of this NPST change also exhibits significant differences between the two QBO phases with a zonally elongated pattern during EQBO winters but separated into two centers during WQBO winters. Diagnoses of the dynamical processes associated with the NPST change indicate the dominant roles of the baroclinic energy conversion and downstream energy propagation. The analysis of intraseasonal flow change indicates a larger amplitude of the MJO-related baroclinicity over the North Pacific. This is likely due to a stronger MJO and associated Rossby wave source in EQBO winters, which may give rise to the enhanced amplitude of the NPST change. On the other hand, different spatial distribution of the NPST change is likely a result of a direct impact of the QBO on the NPST. These results suggest that the QBO impact needs to be considered for better reproduction of the MJO-NPST teleconnection in general circulation models, which may also benefit subseasonal prediction of extratropical storm activities.

1. Introduction

Storm tracks are defined as the preferred regions of extratropical synoptic-scale disturbances. In the Northern Hemisphere, they are centered at the North Pacific and the North Atlantic (Blackmon, 1976). The North Pacific storm track (NPST) plays a critical role in the weather and climate variability in the midlatitudes. Synoptic-scale events such as extreme precipitation (Colle et al., 2008; Kunkel et al., 2012; Salathé, 2006) and heat/cold events (Chang et al., 2016) over North America can result from heat/moisture transport associated with the NPST. Subseasonal variations of some prominent modes of winter midlatitude variability such as the North Atlantic Oscillation (Li, 2011) and North Pacific Oscillation-West Pacific teleconnection patterns (Linkin & Nigam, 2008) are also influenced by the NPST. As such, better understanding of the spatio-temporal variability of the NPST and its possible mechanism is important for improving our understanding and prediction capability of the midlatitude weather and climate variability.

The Madden-Julian Oscillation (MJO; Madden & Julian, 1971, 1972, 1994) is the dominant intraseasonal mode in the tropics with a period ranging from approximately 30 to 60 days. A lot of attention has been paid to the effect of the MJO on tropical atmospheric and oceanic variation since its discovery (e.g., Lau & Waliser, 2011; Zhang, 2005; Zhang et al., 2013). A global impact of the MJO has also been realized since the finding of teleconnections between the tropical heating and the extratropical variation in the early 1980s (Horel & Wallace, 1981; Hoskins & Karoly, 1981). It is well documented that the emanation of a poleward and eastward propagating Rossby wave train in the upper troposphere, excited by the anomalous diabatic heating in the tropics, can effectively modulate extratropical circulations (e.g., Wallace & Gutzler, 1981).

The MJO-midlatitude teleconnection has been analyzed widely from the observational/reanalysis data, modeling, and forecasting perspectives. It has been reported that the MJO strongly modulates the midlatitude weather and climate systems such as blocking frequency (Henderson et al., 2016), extreme precipitation (Mundhenk et al., 2016), North Atlantic Oscillation (Cassou, 2008; Lin et al., 2009), East Asia-Pacific (Wang et al., 2016), and Pacific/North American patterns (Mori & Watanabe, 2008). A detailed review on the tropical-extratropical teleconnections on intraseasonal timescale is offered by Stan et al. (2017).

While considerable progress has been made to delineate the tropical-extratropical teleconnection, less effort has been paid to investigate the relationship between the MJO and storm tracks until recently (Deng & Jiang, 2011; Guo et al., 2017; Lee & Lim, 2012; Takahashi & Shirooka, 2014). It is found that when the enhanced MJO convection is located in the Indian Ocean, a dipole change in the NPST is seen about two weeks later, with enhanced storm-track activity (STA) to the north and reduced STA to the south of its climatological maximum during boreal winter. An opposite change in the NPST is found when the active MJO convection is located over the western Pacific. Not only the north-south displacement of the NPST but also its zonal shift is sensitive to MJO phases (Lee & Lim, 2012). The close relationship between the MJO and NPST holds not only for the Eulerian representatives of the STA (i.e., band-pass-filtered statistics; Deng & Jiang, 2011; Takahashi & Shirooka, 2014) but also for the Lagrangian representatives of the STA (i.e., cyclone tracking; Guo et al., 2017).

The MJO-NPST relationship shows a significant dependence on the background state such as the El Niño-Southern Oscillation (ENSO). Takahashi and Shirooka (2014) demonstrated that when the enhanced MJO convection is located over the Indian Ocean-Maritime continent, the STA over the western (eastern) North Pacific intensifies during La Niña (El Niño) winters. The MJO-NPST relationship also changes by ENSO when the active MJO convection moves to the western-central Pacific. While previous studies primarily examined the modulation of ENSO on the MJO (e.g., Hendon et al., 2007; Moon et al., 2011; Nakazawa, 2000; Pohl & Matthews, 2007), a recent study demonstrated a possible relationship between the MJO and the quasi-biennial oscillation (QBO; Yoo & Son, 2016). The QBO is an interannual phenomenon in the tropical stratosphere that is characterized by a continuous oscillation of easterly and westerly zonal winds with a mean period of about 28 months (Baldwin et al., 2001). It is suggested that the MJO activity is generally stronger (weaker) during easterly (westerly) QBO winters. This QBO-MJO relationship is further confirmed by several recent studies using various MJO metrics (Marshall et al., 2017; Nishimoto & Yoden, 2017; Son et al., 2017; Zhang & Zhang, 2018). According to Son et al. (2017), the QBO seems to play a larger role in the interannual variability of the MJO amplitude than ENSO does. Specifically, while ENSO mainly modulates the MJO variation over the central Pacific, the QBO influences the MJO variation in the Indo-Pacific region from about 60°E to 180° where the MJO tends to be active during boreal winter.

Inspired by the recently discovered QBO-MJO relationship, the present study proposes a hypothesis that the QBO may influence the MJO-NPST relationship through its modulation of tropical convection and associated extratropical circulations. This hypothesis is tested by investigating the MJO-associated intraseasonal flow. The key dynamical processes that are responsible for the MJO-NPST relationship are also examined by diagnoses of energy conversion and energy flux (EF). The rest of the paper is organized as follows. Section 2 contains an introduction of the data sets and statistical metrics used to define the NPST, MJO, QBO, and ENSO. Section 3 describes the MJO-NPST relationship and its modulation by the QBO. The dynamical processes of the QBO-MJO-NPST relationship are presented in section 4. Section 5 discusses the plausible contributors to the QBO-MJO-NPST relationship, followed by a summary and discussion in section 6.

2. Data and Method

2.1. Data

The European Centre for Medium-Range Weather Forecasts Interim reanalysis (ERA-Interim) data set (Dee et al., 2011) is used in the present study. Specifically, daily averaged pressure-level data from 1979 to 2016 including horizontal winds, air temperature, and geopotential with a horizontal resolution of 2.5° longitude × 2.5° latitude are used. The surface quantities, such as sea level pressure (SLP) and surface pressure, are also used. The daily mean outgoing longwave radiation (OLR) data derived from the National Oceanic and Atmospheric Administration with a spatial resolution of 2.5° is used as a proxy of convection. We used the interpolated OLR data from 1979 to 2013 and noninterpolated data from 2014 to 2016. We will focus our analysis on NPST peak season from October to March (hereafter, referred to as “boreal winter”).

The Real-time Multivariate MJO (RMM) index (Wheeler & Hendon, 2004) is used to characterize the phase and amplitude of the MJO. The RMM1 and RMM2 indices are the first and second principal components (PC1 and PC2) of the combined empirical orthogonal functions of OLR, 850-hPa and 200-hPa zonal wind averaged from 15°S to 15°N. Both RMM1 and RMM2 indices are obtained from the website (http://www.bom.gov.au/climate/mjo). To test the robustness of the results, the OLR-based MJO index (OMI; Kiladis et al., 2014) is also compared (https://www.esrl.noaa.gov/psd/mjo/mjoindex/). All the results in this study are the composites of strong MJO events, which are defined as $\sqrt{PC1^2 + PC2^2}$ larger than 1.0 (an approximation of one standard deviation for each PC; Wheeler & Hendon, 2004).

Different phases of the QBO are determined by the normalized tropical-mean (10°S–10°N) 50-hPa zonal wind (U50) anomalies calculated by the ERA-Interim data, which incorporate the actual radiosonde zonal wind (Dee et al., 2011). For seasonal-mean U50 larger than 0.5 standard deviation, the corresponding boreal winter is regarded as the westerly phase of the QBO (WQBO). Likewise, for U50 smaller than -0.5 standard deviation, the corresponding winter is defined as an easterly QBO (EQBO) winter (Son et al., 2017; Yoo & Son, 2016). Based on this criterion, 18 out of 37 winters are selected as WQBO winters and 12 as EQBO winters.

ENSO phases are determined by the seasonal-mean Niño-3.4 index calculated by the Extended Reconstructed Sea Surface Temperature, version 4 (Huang et al., 2015). El Niño events are defined by the Niño-3.4 index larger than 0.8 K (one standard deviation), while La Niña events correspond to the Niño-3.4 index less than -0.8 K. Out of 37 winters, 9 El Niño events and 9 La Niña events are selected.

2.2. Methodology

Although previous studies suggest a relationship between the MJO and the NPST, the results are based mostly on single-statistic representatives of storm tracks (e.g., Deng & Jiang, 2011; Takahashi & Shirooka, 2014). To test the robustness of our results, three statistical metrics are used to identify the NPST. The first metric is the 24-hr difference-filtered variance of 300-hPa meridional wind (vv300; Chang et al., 2012; Chang & Yau, 2016; Wallace et al., 1988) calculated as

$$\mathrm{vv300} = (v(t + 24\ \mathrm{hr}) - v(t))^2 \tag{1}$$

Because the disturbances shorter than two days is relatively small, this 24-hr difference could be regarded as a high-pass filter that passes full power at two days and half power at six days (Wallace et al., 1988). The second metric is the 2- to 8-day filtered variance of daily SLP (*pp*; Chang et al., 2012). To derive the *pp*, a 2- to 8-day Lanczos filter (Duchon, 1979) is applied first to daily SLP. Then, the square of the filtered quantities is obtained. The third metric is the eddy kinetic energy (EKE) averaged from 950 to 250 hPa (Deng & Jiang, 2011; Takahashi & Shirooka, 2014), which is expressed as

$$\mathrm{EKE} = \frac{1}{2}\left(u'^2 + v'^2\right) \tag{2}$$

where u and v are the zonal and meridional wind, respectively, and prime indicates the synoptic-scale (2–8 days) variability. Before the computation of the EKE, a 2- to 8-day Lanczos filter is applied to daily horizontal winds at each pressure level.

Anomalies of all variables are derived by subtracting the seasonal cycle from the total field. A 25- to 90-day Lanczos filter is then applied to extract intraseasonal variability. The Student's *t* test is used to test the significance of the results. Due to the continuity of MJO phases, the degrees of freedom are smaller than actual MJO days that are used for the composite. Therefore, the degrees of freedom are determined as number of days per strong MJO phase divided by 5 (5 days is the average duration of an individual MJO phase; Alaka & Maloney, 2012; Henderson et al., 2016; Henderson et al., 2017).

3. MJO-NPST Relationship and its Modulation by the QBO

The boreal winter NPST variance defined by the variance of daily and intraseasonal (25- to 90-day filtered) EKE anomalies are compared in Figure 1. The NPST shows significant variation in its climatologically active region. The intraseasonal variance (Figure 1b) exhibits nearly identical pattern with the total variance (Figure 1a) albeit with weaker amplitude. The intraseasonal EKE variance averaged over 120°E–120°W, 40°–60°N (blue box in Figure 1b) accounts for approximately 10% of the total variance (Figure 1a), indicating a nonnegligible intraseasonal NPST variation.

To examine the NPST change during individual MJO phases, composites of intraseasonal EKE anomalies averaged over 120°E–120°W, 40°–60°N (blue box in Figure 1b) for each MJO phase are shown in Figure 2. Given the fact that it takes about 10 days for a tropical-forced Rossby wave packet to reach high latitudes (Hoskins & Karoly, 1981), we consider the anomalies averaged between 3 and 10 days after the strong MJO days. This time lag is applied to all MJO-related extratropical variabilities analyzed in this study. Among eight MJO

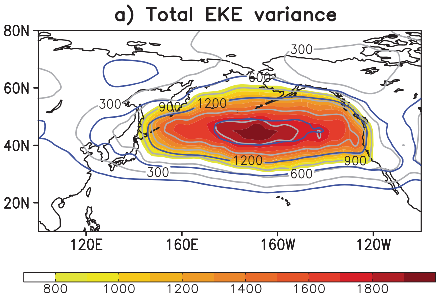

Figure 1. Climatology of (a) seasonal-mean EKE (blue contours, interval: 10 m^2/s^2), variance of EKE (shading and gray contours, unit: m^4/s^4), and (b) variance of 25- to 90-day filtered EKE (shading and gray contours, unit: m^4/s^4). The blue box in (b) represents the area of the northern North Pacific (120°E–120°W, 40°–60°N).

phases, phases 2–3 (enhanced convection over the Indian Ocean) are found to be the dominant contributors to an enhanced EKE over the North Pacific after 3–10 days, while phases 6–8 (active convection over the western to central Pacific) mostly result in a suppressed EKE over the northern North Pacific, consistent with previous studies (e.g., Deng & Jiang, 2011; Takahashi & Shirooka, 2014).

According to the locations of active MJO convection and the similarity between EKE anomalies during certain MJO phases inferred from Figure 2, the NPST changes are grouped into MJO phases 2–3 and 6–8, respectively. Composites of the MJO-associated EKE anomalies are displayed in Figure 3. An increase (decrease) in the EKE on the northern (southern) flank of the NPST is found when the MJO convection is located over the Indian Ocean (Figure 3a). An opposite EKE change is seen when the enhanced convection is in the western to central Pacific (Figure 3b).

To evaluate the robustness of the MJO-NPST relationship, the same analysis is repeated with the other two STA metrics introduced in section 2 (not shown). The centered spatial correlation coefficient (e.g., Taylor, 2001) over 120°E–100°W, 20°–60°N (red box in Figure 3a) for the composites of all winters (i.e., Figures 3a and 3b) is calculated between the three metrics (EKE, vv300, and *pp*; Table 1). It is shown that the averaged correlation coefficients are 0.58 and 0.59 for MJO phases 2–3 and 6–8, respectively, which are statistically significant beyond a 99% confidence level.

As suggested by Yoo and Son (2016) and Son et al. (2017), the QBO strongly regulates the MJO amplitude in the Indo-Pacific region. During EQBO (WQBO) winters, when the enhanced convection is located over the Indian Ocean (Figures 3c and 3e), an elongated and stronger (separated and weaker) EKE anomaly is found in the northern North Pacific. In MJO phases 6–8 (Figures 3d and 3f), similar EKE anomalies are seen but with opposite signs to MJO phases 2–3. These results demonstrate a significant modulation of the MJO-related NPST change by the QBO.

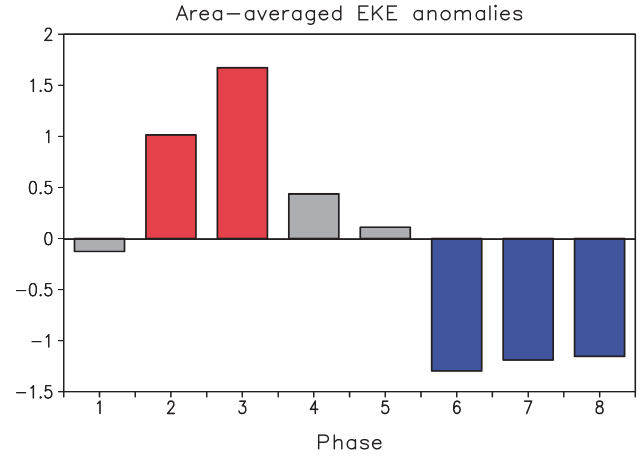

Figure 2. 25- to 90-day filtered EKE anomalies (m^2/s^2) averaged over the northern North Pacific (indicated by the blue box in Figure 1b) for individual MJO phases. The red and blue colored bars indicate significant anomalies exceeding the 95% confidence level.

The same analysis (i.e., Figure 3) has been conducted based on the OMI (not shown). The centered spatial correlation coefficients calculated over 120°E–100°W, 20°–60°N (red box in Figure 3a) between the OMI- and RMM-based results are computed. It turns out that correlation coefficients of EKE anomalies during EQBO winters are 0.64 and 0.69 for MJO phases 2–3 and 6–8, respectively. They are 0.69 and 0.71 during WQBO winters. These numbers are statistically significant beyond a 99% confidence level, suggesting that overall the results are not sensitive to the choice of MJO index.

4. The Dynamical Processes Associated With the NPST Change

4.1. Barotropic and Baroclinic Energy Conversion

Storm tracks are related to the energy conversion between the mean flow and eddies (e.g., Chang et al., 2002). To examine the energy

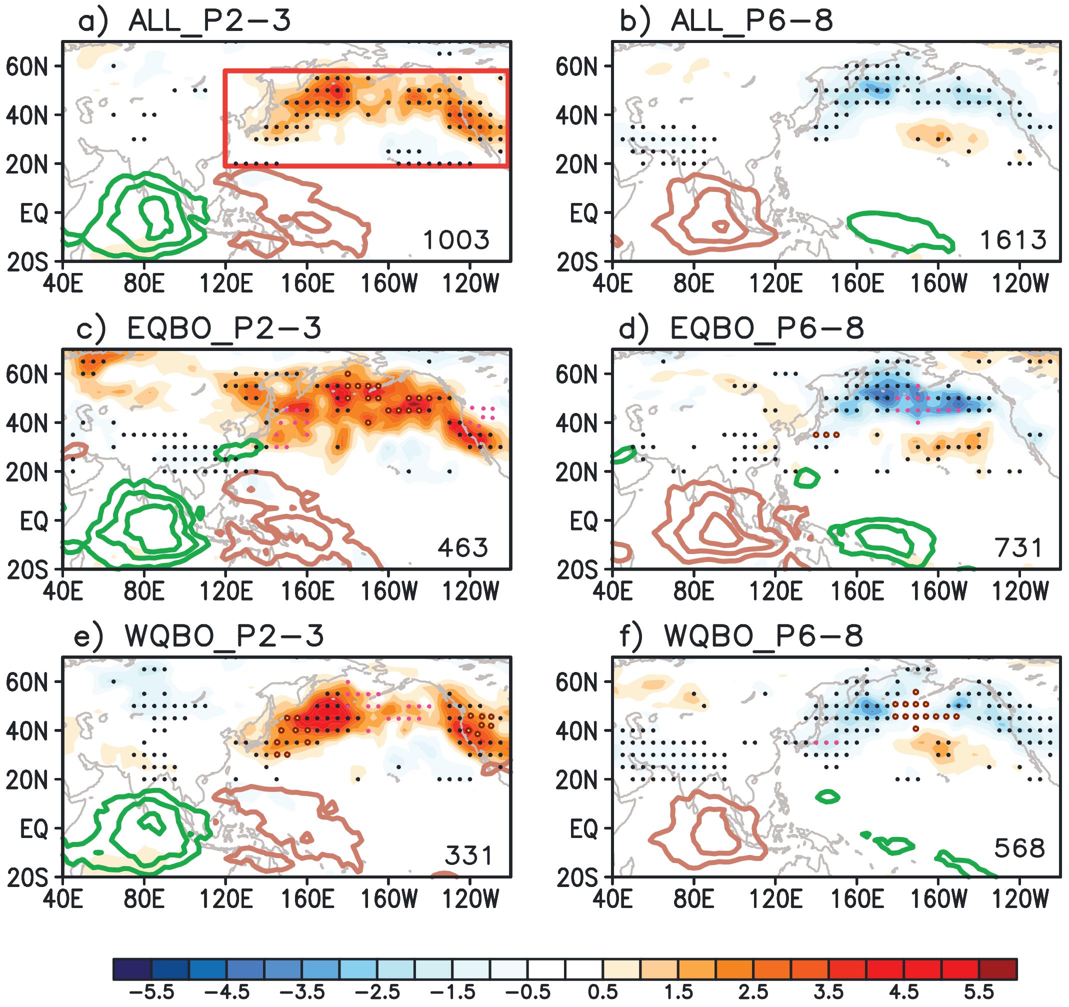

Figure 3. Composites of intraseasonal OLR (contour, unit: W/m^2) and 3- to 10-day lagged EKE (shading, unit: m^2/s^2) anomalies in (left column) MJO phases 2–3 and (right column) phases 6–8 for (a and b) all, (c and d) EQBO, and (e and f) WQBO winters. The green (brown) contours represent negative (positive) OLR anomalies (interval of 5 W/m^2). The dotted areas represent significant EKE anomalies exceeding the 95% confidence level, in which the brown-open (pink-solid) dots represent a significant positive (negative) difference between the two QBO phases (plotted every 5°). Numbers of strong MJO days are indicated in the lower-right corner of each plot. The red box in (a) represents the area for the spatial correlation calculation (120°E–100°W, 20°–60°N).

conversion, mean flow is defined as variability on time scales longer than 9 days and eddy is defined as 2- to 8-day band-pass-filtered variables (i.e., synoptic transients). In this sense, a quantity A could be decomposed as $A = \overline{A} + A'$, where overbar indicates the mean flow and prime represents synoptic transients. Using this decomposition, the barotropic energy conversion (BTEC) between mean kinetic energy and EKE is analyzed using equation (3). We also examine the baroclinic energy conversion (BCEC), which involves energy conversion from mean available potential energy to eddy available potential energy (BCEC1) and from eddy available potential energy to EKE (BCEC2) using equations (4) and (5) (Cai et al., 2007; Dole & Black, 1990; Hoskins et al., 1983; Lee et al., 2012; Simmons et al., 1983):

$$\mathrm{BTEC} = \frac{P_O}{g}\left\{\frac{1}{2}\left(v'^2 - u'^2\right)\left(\frac{\partial\overline{u}}{\partial x} - \frac{\partial\overline{v}}{\partial y}\right) + \left(-u'v'\right)\left(\frac{\partial\overline{v}}{\partial x} + \frac{\partial\overline{u}}{\partial y}\right)\right\} \tag{3}$$

$$\mathrm{BCEC1} = \left(\frac{\frac{P_0}{P}\frac{R}{g}}{\frac{d\theta}{dp}}\right)\left(u'T'\frac{\partial\left(\overline{T}\right)}{\partial x} + v'T'\frac{\partial\left(\overline{T}\right)}{\partial y}\right) \tag{4}$$

Table 1
Cross Spatial Correlation Between the Different Representatives of the North Pacific Storm Track (NPST) Over 120°E–100°W, 20°–60°N (Red Box in Figure 3a) for Combined MJO Phases

MJO phases	2–3	6–8
EKE and *pp*	0.54	0.56
pp and vv300	0.38	0.38
vv300 and EKE	0.82	0.81
Average	0.58	0.59

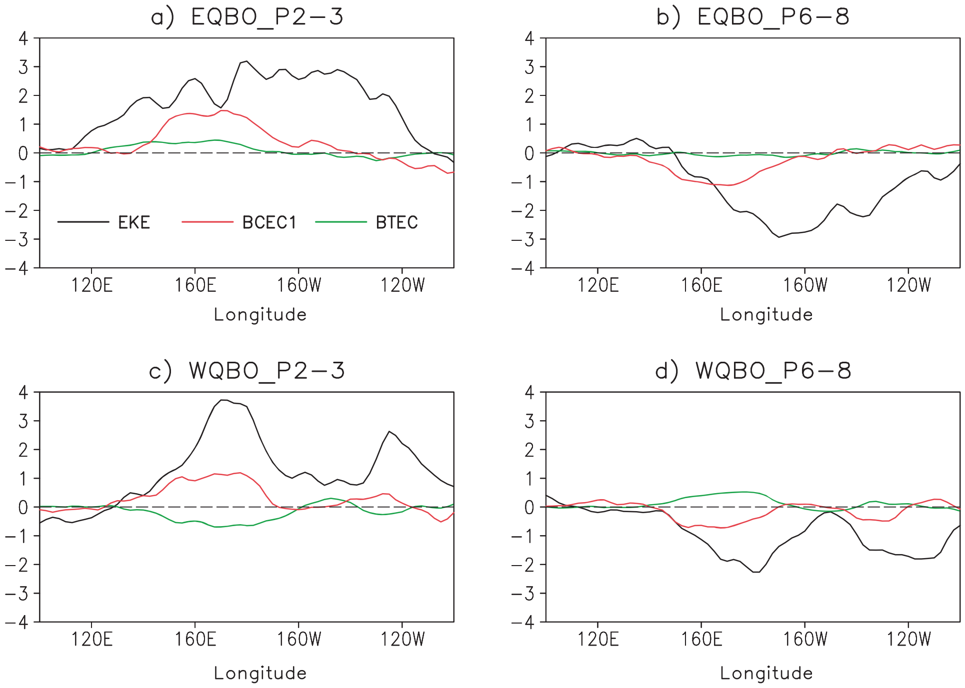

Figure 4. Longitudinal variation of 40°–60°N averaged and vertically averaged (950 to 250 hPa) intraseasonal EKE (m^2/s^2), barotropic energy conversion (BTEC; $m^2 \cdot s^{-2} \cdot day^{-1}$), and baroclinic energy conversion from mean available potential energy to eddy available potential energy (BCEC1) anomalies ($m^2 \cdot s^{-2} \cdot day^{-1}$) during (a and c) MJO phases 2–3 and (b and d) phases 6–8 in (a and b) EQBO and (c and d) WQBO winters.

$$\mathrm{BCEC2} = -\left(\frac{P_0}{P}\right)^{C_v/C_p} \frac{R}{g}\left(\omega' T'\right) \tag{5}$$

Here g is the gravitational acceleration, P_o is the reference pressure (1,000 hPa), θ denotes potential temperature, R (287 $J \cdot kg^{-1} \cdot K^{-1}$) is the gas constant for dry air, and C_v (717 $J \cdot kg^{-1} \cdot K^{-1}$) and C_p (1,004 $J \cdot kg^{-1} \cdot K^{-1}$) are the specific heat of dry air at constant volume and pressure, respectively. The BTEC is related to the interactions between the deformation of the basic flow and eddy momentum fluxes as indicated by equation (3). The BCEC1 is related to horizontal eddy heat flux and mean horizontal temperature gradient (equation (4)), whereas the BCEC2 is an indication of vertical eddy heat flux (equation (5)). Only results of the BCEC1 are shown in this study since the patterns of the BCEC2 are nearly identical to the BCEC1. Note that in the classical baroclinic eddy life cycle calculation (Simmons & Hoskins, 1978), the BCEC1 is followed by the BCEC2, converting mean available potential energy of the system to the EKE. The resulting EKE tends to barotropically decay.

To determine the relative contribution of the BTEC and BCEC in the NPST change, the longitudinal variations of 40°–60°N averaged intraseasonal EKE, BTEC, and BCEC1 anomalies averaged from 950 to 250 hPa in the two QBO phases are compared in Figure 4. The zonally elongated (separated) distribution of the MJO-related NPST change during EQBO (WQBO) winters is clearly seen from EKE anomalies in both MJO phases 2–3 and 6–8. This spatial distribution difference is associated with changes in the BCEC rather than the BTEC. For instance, in EQBO winters (Figures 4a and 4b), a strengthening (weakening) in the BCEC1 over 135°E–150°W matches the increase (decrease) in the EKE during MJO phases 2–3 (phases 6–8). However, the BTEC anomalies in this region are negligibly small. Note that the spatial patterns of the BCEC1 do not match exactly with the EKE anomalies. During EQBO winters (Figures 4a and 4b), while the BCEC1 is maximized around the date line, the EKE exhibits a much broader distribution in longitudes. During WQBO winters (Figures 4c and 4d), largest BCEC1 anomalies are commonly found upstream of the maximum EKE anomalies. These differences are discussed later in terms of the EF.

The detailed spatial distribution of BCEC1 anomalies is further illustrated in Figure 5. The increase (decrease) in the EKE is consistent with positive (negative) BCEC1 anomalies (Figures 5a and 5b). The modulation of the

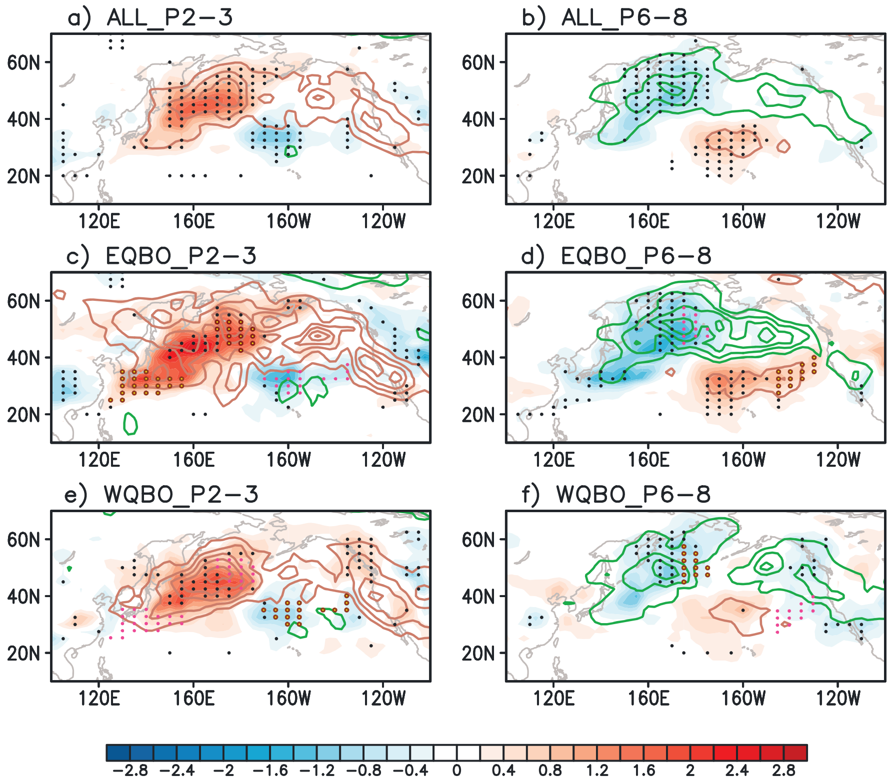

Figure 5. Same as Figure 3, except for the intraseasonal BCEC1 (shading, unit: $m^2 \cdot s^{-2} \cdot day^{-1}$) and EKE anomalies (colored contour, interval: 1 m^2/s^2) averaged from 950 to 250 hPa. The brown (green) contours represent positive (negative) EKE anomalies. The dotted areas indicate significant BCEC1 anomalies exceeding the 95% confidence level, in which the brown-open (pink-solid) dots represent a significant positive (negative) difference between the two QBO phases (plotted every 5°).

MJO-related NPST change by the QBO is indicated to be closely related to the BCEC1 as well (Figures 5c–5f). The zonally elongated (separated) distribution of the NPST change in EQBO (WQBO) winters are well captured by BCEC1 anomalies.

To evaluate the relative importance of eddy-mean flow interaction on different time scales, the first term of the BCEC1 is decomposed into intermediate (9–24 days), intraseasonal (25–90 days), and low-frequency (>90 days) contributions. The results of the projection coefficient (Feldstein, 2002) between the decomposed terms and EKE anomalies suggest a dominant role of the interaction between storm-track eddies and low-frequency flow (not shown).

Since the meridional component of the BCEC1 is always larger than its zonal component, intraseasonal $v'T'$ may be the major contributor to the BCEC1. Indeed, the spatial distribution of $v'T'$ anomalies has large similarity with the overall pattern of the BCEC1 (Figure 6) than $u'T'$ (not shown). Positive (negative) BCEC1 anomalies generally coincide with an increased (decreased) $v'T'$, consistent with Takahashi and Shirooka (2014). The most significant $v'T'$ is always generated within or near the region of maximum low-frequency baroclinicity, $-\frac{\partial(\overline{T})}{\partial y}$ (Figure 6). These results suggest that the MJO-related intraseasonal $v'T'$ fluctuated on the low-frequency background flow is the primary contributor to the variation of the NPST.

4.2. Downstream Energy Propagation

In the previous section, we found that the energy source/sink in EQBO winters is not as broad as the distribution of EKE anomalies (e.g., Figures 5c and 5d). In other words, the maximum of the BCEC1 is only found in the northwestern Pacific instead of the entire North Pacific. To investigate how energy is redistributed from the energy source/sink to the downstream region, analysis of the EF is conducted using the formula developed by Orlanski and Sheldon (1993) and modified by Chang and Orlanski (1994):

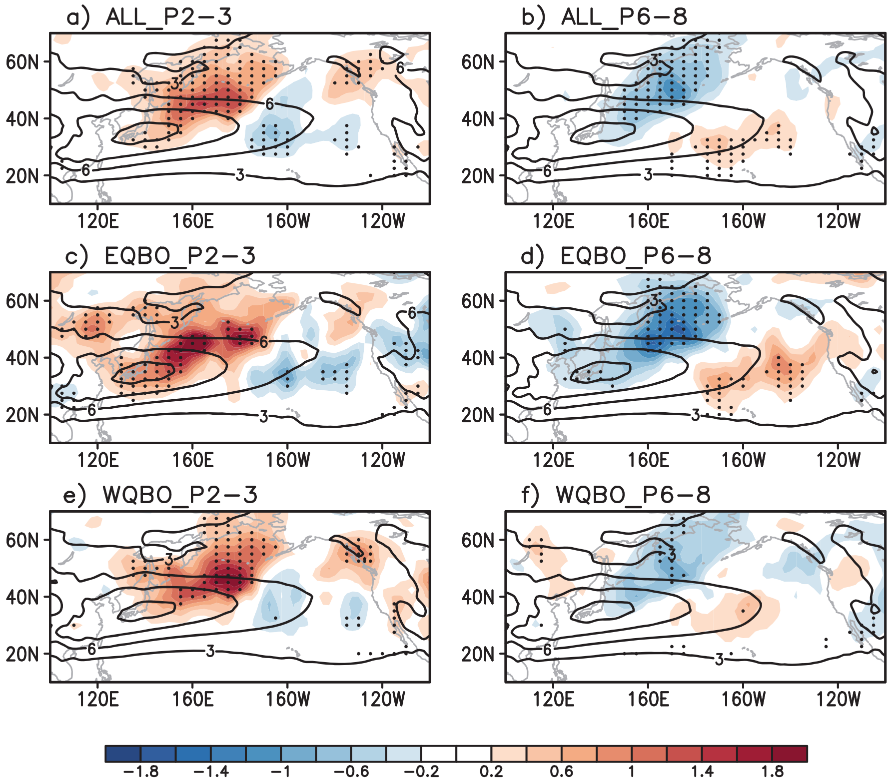

Figure 6. Same as Figure 3 except for intraseasonal meridional heat flux $v'T'$ anomalies (shading, unit: K m · s^{-1}) and low-frequency baroclinicity $-\frac{\partial(\overline{T})}{\partial y}$ averaged from 950 to 250 hPa (contour, interval: 3 × 10^{-5} K/m). The dotted areas indicate significant $v'T'$ anomalies exceeding the 95% confidence level (plotted every 5°).

$$\mathrm{EF}=\begin{cases}\overline{u}\mathrm{EKE}+u_a{'}\phi{'}-\dfrac{\partial}{\partial y}\left(\dfrac{\beta y\psi'^2}{2}\right)\\[2ex]\overline{v}\mathrm{EKE}+v_a{'}\phi{'}+\dfrac{\partial}{\partial x}\left(\dfrac{\beta y\psi'^2}{2}\right)\end{cases}\tag{6}$$

where the subscript "a" represents the ageostrophic components of the horizontal winds, ϕ is the geopotential, and ψ is the streamfunction. The first term is the advective EF, which denotes energy advection by the mean flow; the second is the ageostrophic geopotential flux, which indicates energy dispersion; and the third represents circulation of energy around the high/low energy centers. As suggested by Chang and Orlanski (1994), the modified EF indicates the direction of eddy propagation and is equal to the product of the group velocity and the eddy energy in the Wentzel-Kramers-Brillouin limit. The climatological convergence center of the EF is found downstream of the BCEC1 maximum (Figure 9 in Chang et al., 2002), suggesting a redistribution of energy from the region where the energy is generated to the downstream regions (known as "downstream development"). Given the fact that the efficiency of downstream development is dependent on the background flow (e.g., Son et al., 2009), it is plausible that the MJO-related background flow change can modulate EF anomalies.

Intraseasonal EF anomalies, averaged from 950 to 250 hPa, are shown in Figure 7. In all winters, a continuous downstream energy propagation is discerned for MJO phases 2–3 (Figure 7a) when an energy source exists over the northwestern Pacific (Figure 5a). As a comparison, the direction of energy transport anomalies on the northern flank of the NPST is in an opposite sign for MJO phases 6–8 (Figure 7b). The continuous energy transport may drive an extension of EKE anomalies from the energy source/sink to its downstream regions and result in an elongated distribution of EKE anomalies (Figures 3a and 3b). The comparison between MJO phases 2–3 and 6–8 (Figures 7a and 7b) further suggests an interesting feature. The magnitude of

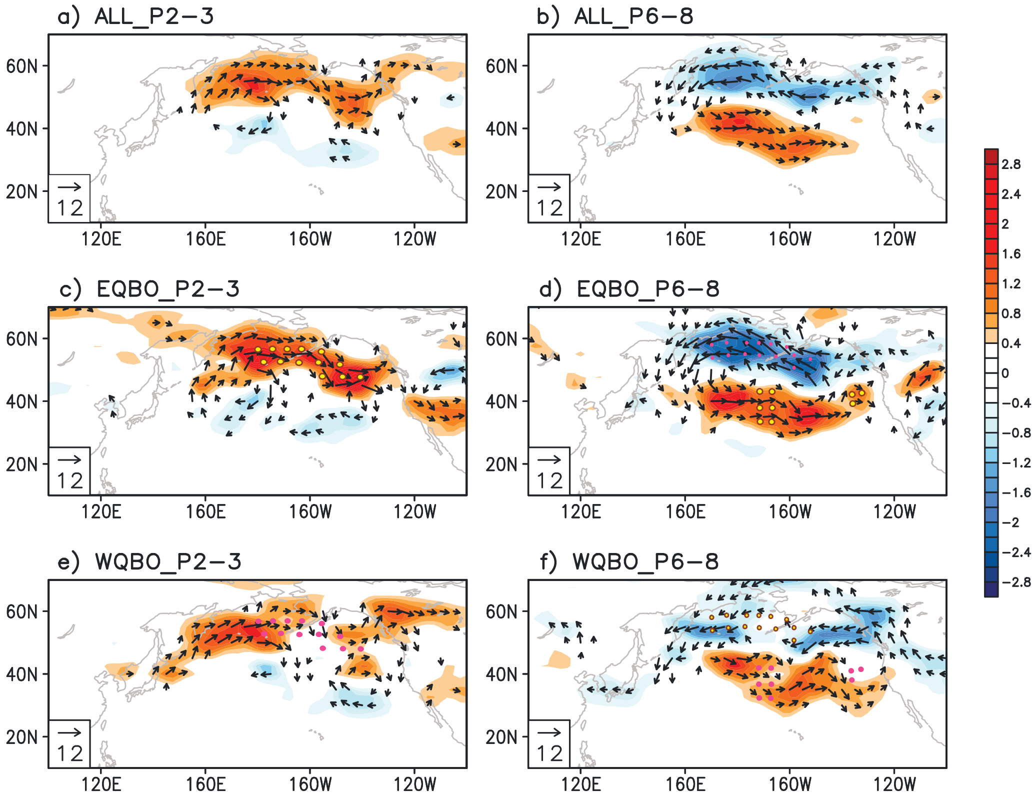

Figure 7. Same as Figure 3 except for the intraseasonal energy flux anomalies averaged from 950 to 250 hPa (vector, unit: m^3/s^3). Only significant vectors exceeding the 95% confidence level are shown. Shading represents the zonal component of the energy flux. The brown-open (pink-solid) dots represent a significant positive (negative) difference between the two QBO phases (plotted every 5°).

energy transport over the northern and southern flank of the NPST is comparable for phases 6–8 while a large north-south asymmetry in magnitude is found for phases 2–3. This difference is likely responsible for the stronger EKE anomalies over the southern flank of the NPST as observed in MJO phases 6–8 (Figure 3b) than in phases 2–3 (Figure 3a) even though the amplitude of energy generation/dissipation is comparable (Figures 5a and 5b).

The energy propagation in EQBO winters (Figures 7c and 7d) appears to be more continuous and stronger than that in all winters. On the contrary, a disrupted energy transport is seen over the northern side of the climatological NPST in WQBO winters (Figures 7e and 7f). A stronger meridional transport in the middle of the North Pacific interrupts the continuous zonal transport, which is much more significant for MJO phases 2–3. As a result, two propagation centers are found with one over the northwestern Pacific (120°E–180°) and the other over the northeastern Pacific (130°W–100°W) in WQBO winters, which matches the two-peak distribution of EKE anomalies. Convergence of the EF (not shown) generally indicates a downstream development of the EKE with a divergence (convergence) center upstream (downstream) of BCEC1 anomalies. It is found that the three terms in equation (6) have comparable contribution to the zonal component of the EF while changes in the meridional component are mainly a result of $\frac{\partial}{\partial x}\left(\frac{\beta y \psi'^2}{2}\right)$, which represents the circulation of energy.

5. The Plausible Contributors to the QBO-MJO-NPST Relationship

5.1. Amplitude of the NPST Change

In section 3, a larger amplitude of the MJO-related NPST change is found in EQBO than WQBO winters. To examine the role of the MJO and its associated intraseasonal flow in the NPST amplitude difference,

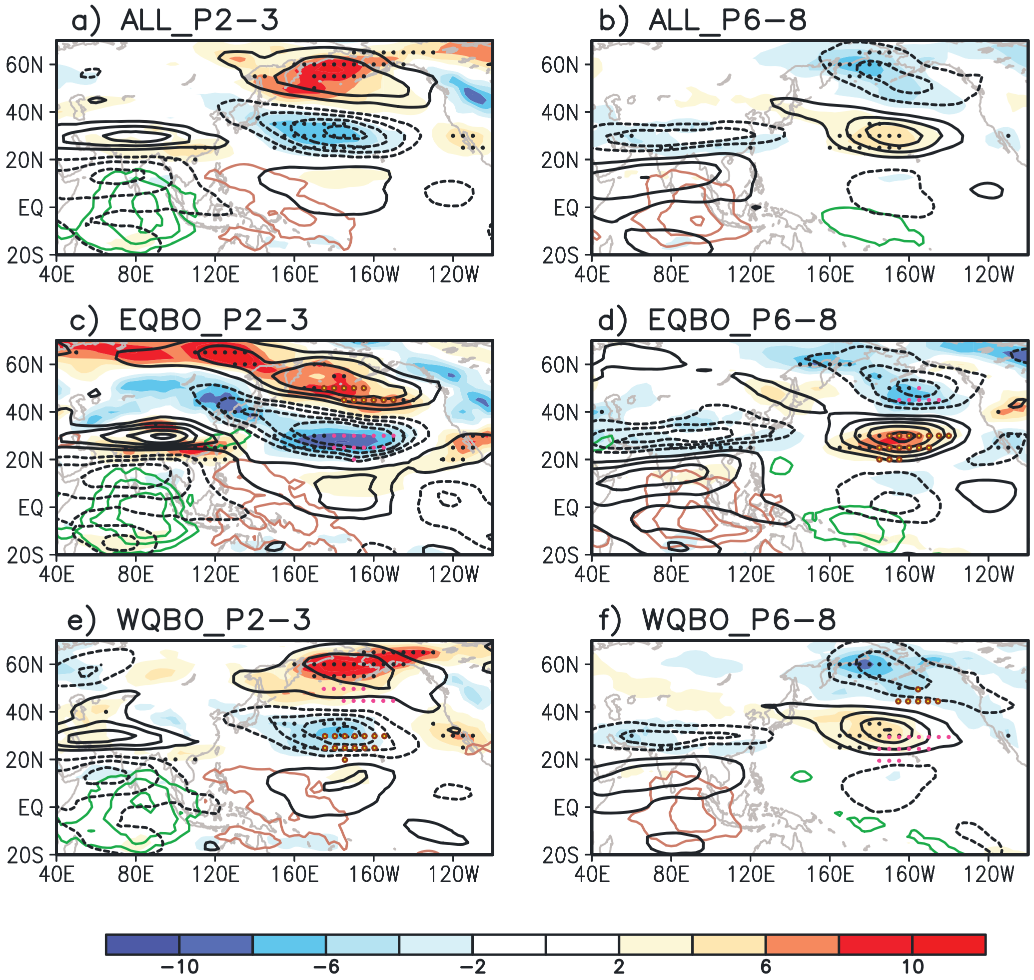

Figure 8. Same as Figure 3 except for the intraseasonal 300-hPa zonal wind (black contour, interval: 1 m/s) and 950–250 hPa averaged baroclinicity (shading, unit: 10^{-6} K/m) anomalies. The dotted areas indicate significant baroclinicity anomalies exceeding the 95% confidence level, in which the brown-open (pink-solid) dots represent a significant positive (negative) difference between the two QBO phases (plotted every 5°).

300-hPa zonal wind (U300) is analyzed. Because the genesis of midlatitude cyclones is strongly controlled by baroclinic instability (Eady, 1949), baroclinicity represented by the negative meridional temperature gradient ($-\frac{dT}{dy}$) is also examined. Here y is the meridional Cartesian coordinate with positive northward. The baroclinicity $-\frac{dT}{dy}$ averaged from 950 to 250 hPa is displayed together with U300 in Figure 8. Not surprisingly, changes of anomalous U300 are consistent with that of anomalous baroclinicity. For instance, when the extratropical baroclinic zone shifts northward, the North Pacific westerly jet shifts northward accordingly (Figure 8a).

Changes of intraseasonal flow suggest a significant modulation of the NPST by the MJO-associated baroclinicity (Figures 3 and 8). During MJO phases 2–3, the enhancement of baroclinicity to the north of the climatological NPST and an attenuation to the south (Figure 8a) are consistent with a poleward shift of the NPST (Figure 3a). In MJO phases 6–8, baroclinicity anomalies over the North Pacific (Figure 8b) well match a southward shift of the NPST (Figure 3b). Although the MJO-NPST relationship shown in Figure 3 is significantly associated with the extratropical intraseasonal flow changes, the meridional asymmetry of the NPST changes (i.e., much stronger changes over 40°–60°N than over 30°–40°N in Figures 3a and 3b) could hardly be explained by the relatively symmetric amplitude of baroclinicity changes (Figures 8a and 3b). In other words, the magnitude of changes on the southern flank of the NPST is always weaker than that on the northern flank, although the baroclinicity changes over these two regions are comparable. This suggests that the linear baroclinicity can only explain the difference in the northern flank of the NPST change. This is confirmed by previous studies that baroclinicity alone cannot fully explain the different magnitude changes between the northern and southern flanks of the storm track, yet no underlying mechanism has been proposed (e.g., Athanasiadis et al., 2010; Brayshaw et al., 2011; Guo et al., 2017; Woollings et al., 2012).

The comparison between the two different QBO phases suggests stronger baroclinicity (and U300) anomalies over the North Pacific in EQBO than WQBO winters (Figures 8c–8f). Enhanced baroclinicity anomalies in the high latitudes (Figures 8c and 8d) may explain the stronger EKE anomalies under EQBO condition (Figures 3c and 3d). It is also found that the westerly jet is weaker around 30°N and wider in EQBO winters (not shown; Garfinkel & Hartmann, 2011; Seo et al., 2013). As suggested by Harnik and Chang (2004), the wider but weaker westerly jet may result in a stronger NPST due to a decrease in group velocity and an enhancement in temporal growth rate. Therefore, both the intensification of the intraseasonal baroclinicity in the high latitudes and the meridional broadening of the westerly jet stream in the midlatitudes during EQBO winters likely account for the larger amplitude of the NPST response to the MJO.

To better understand stronger MJO-related extratropical circulation anomalies in EQBO winters, the Rossby wave source (RWS) is analyzed. Following Sardeshmukh and Hoskins (1988), the RWS is expressed as follows:

$$\mathrm{RWS} = -\boldsymbol{V}_{\chi}\cdot\nabla\xi - \xi\nabla\cdot\boldsymbol{V}_{\chi} \tag{7}$$

where $\boldsymbol{V}_{\chi}$ represents the divergent wind and ξ denotes the absolute vorticity. As demonstrated by equation (7), the RWS consists of an advection term (more precisely the absolute vorticity advection by the divergent winds) and a divergence term. A positive RWS corresponds to a cyclonic vorticity generation in the Northern Hemisphere and vice versa for a negative RWS (Sardeshmukh & Hoskins, 1988).

The intraseasonal RWS anomalies at 300 hPa are illustrated in Figure 9. During MJO phases 2–3 (Figure 9a), negative RWS is found over South to East Asia, indicating a generation of anticyclonic anomaly over the northern North Pacific (implied in Figure 8a). The opposite is true for MJO phases 6–8 (Figure 9b). A comparison between the two QBO phases reveals a stronger RWS in EQBO winters than in WQBO winters (Figures 9c–9f), consistent with the observed difference in the intraseasonal flow (Figures 8c–8f).

The RWS can be linearized and decomposed into the following form (e.g., Hsu, 1996; Seo & Lee, 2017; Takahashi & Shirooka, 2014):

$$\mathrm{RWS} = \left(-\overline{\xi}\nabla\cdot{\boldsymbol{V}_{\chi}}^{IS} - \xi^{IS}\nabla\cdot\overline{\boldsymbol{V}_{\chi}}\right) + \left(-{\boldsymbol{V}_{\chi}}^{IS}\cdot\nabla\overline{\xi} - \overline{\boldsymbol{V}_{\chi}}\cdot\nabla\xi^{IS}\right) \tag{8}$$

where the superscript “IS” represents the intraseasonal anomalies and the overbar denotes the seasonal mean. The RWS generated by $-\overline{\xi}\nabla\cdot{\boldsymbol{V}_{\chi}}^{IS}$ (the first term on the right-hand side of equation (8)) has nearly identical spatial distribution and equivalent magnitude to the RWS (not shown), indicating its dominant contribution to the RWS. This suggests that the difference in the RWS between the two QBO phases (Figures 9c–9f) results either from the seasonal-mean background absolute vorticity ($\overline{\xi}$) change or from the MJO-induced intraseasonal divergence ($-\nabla\cdot{\boldsymbol{V}_{\chi}}^{IS}$) change. Analysis of $\overline{\xi}$ indicates that it is generally weaker during EQBO than WQBO winters (not shown), which is opposite to the RWS difference. Therefore, the observed difference in the RWS is more likely caused by the difference in the MJO-related divergence. To test this possibility, intraseasonal 300-hPa velocity potential anomalies are examined in Figure 9 (black contour). In EQBO winters, the upper-level divergence (convergence) over the Indian Ocean is stronger than that in WQBO winters for phases 2–3 (phases 6–8; Figures 9c–9f). This may be attributed to the stronger MJO activity in EQBO winters (Figures 3c and 3d), although more detailed analysis is needed to examine the potential source of the different extratropical circulation.

5.2. Spatial Distribution of the NPST Change

The above section suggests that the MJO-related NPST anomalies substantially differ between the two QBO phases likely due to changes in the MJO amplitude and its associated intraseasonal flow. However, it is unclear what may contribute to the difference in the spatial distribution of the NPST anomalies, that is, the zonally elongated (separated) EKE anomalies in EQBO (WQBO) winters.

To evaluate the role of the MJO amplitude in the EKE-anomaly distribution, we compare the NPST anomalies for extreme strong MJO events (amplitude >2.0) and medium strong MJO events (amplitude from 1.0 to 2.0) separately for MJO phases 2–3 (Figure 10). In EQBO (WQBO) winters, the elongated (separated) distribution of the NPST change is always found no matter how strong the MJO is. The same results are found when only

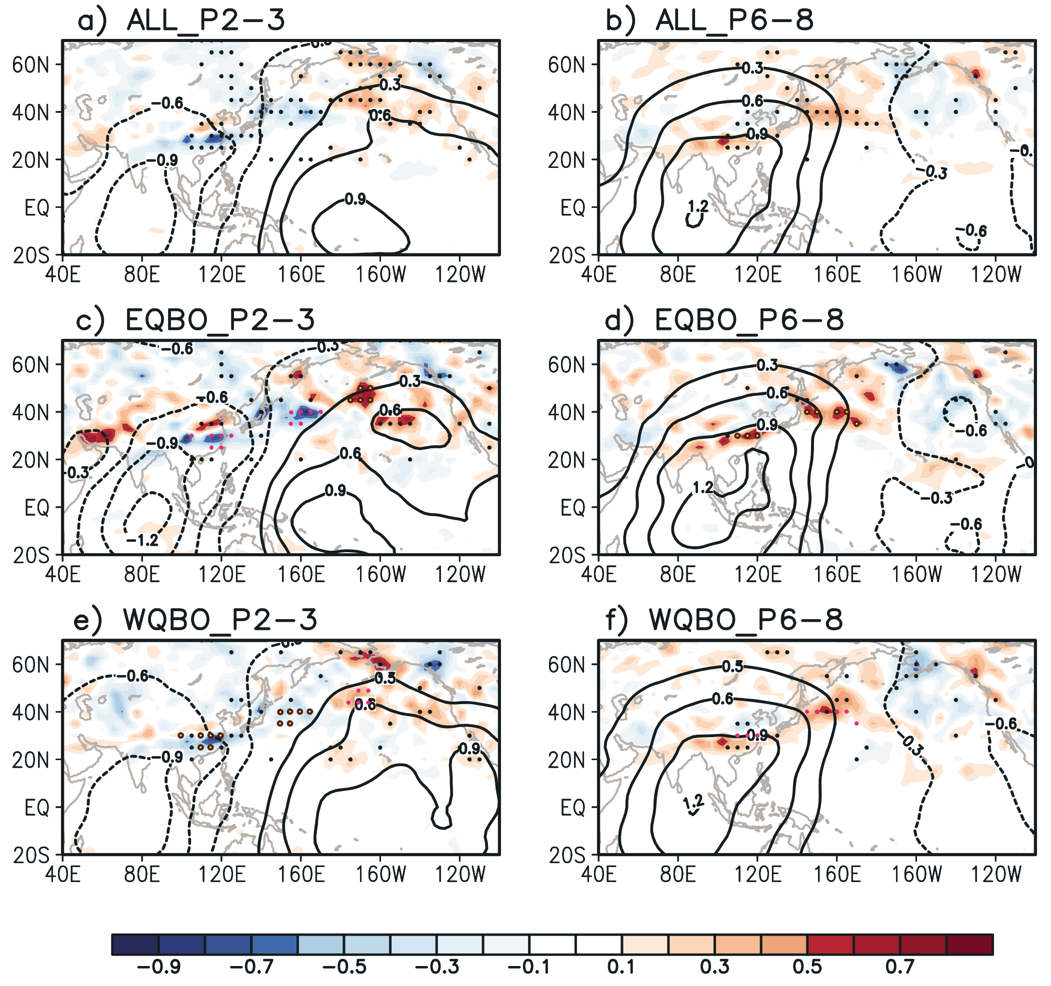

Figure 9. Same as Figure 3 except for the 300-hPa intraseasonal Rossby wave source (RWS; shading, unit: 10^{-10} s^{-2}) and velocity potential (contour, unit: 10^6 m^2/s) anomalies. The dotted areas indicate significant RWS anomalies exceeding the 95% confidence level (plotted every 5°). The brown-open (pink-solid) dots represent a significant positive (negative) difference between the two QBO phases (the dots are shown when difference between the RWS and velocity potential has the same sign).

MJO amplitudes of 1.5 to 2.0 are considered (not shown). The same conclusion is also drawn for MJO phases 6–8 (not shown). This suggests that the spatial distribution of the MJO-related NPST change may not be influenced by the MJO amplitude but is likely caused by the QBO.

A possible candidate that may be responsible for the observed spatial distribution difference in the NPST is the variation of the seasonal-mean NPST modulated by the QBO. Over the region where the MJO most strongly modulates the NPST (40°–60°N, 130°E–120°W), the seasonal-mean NPST is stronger during EQBO winters (Figure S1a in Wang et al., 2018); hence, there could be a stronger MJO modulation on the NPST. While during WQBO winters, the seasonal-mean NPST is weaker especially between 180° and 150°W (Figure S1b in Wang et al., 2018); hence, the MJO modulation may be weaker. This difference may lead to an elongated (separated) intraseasonal EKE distribution in EQBO (WQBO) winters. However, this explanation is incomplete and the causal relationship merits further investigation.

6. Summary and Discussion

The present study investigates the modulation of the MJO-NPST relationship by the QBO using reanalysis data with a specific focus on boreal winter (October to March) from 1979 to 2016. On intraseasonal

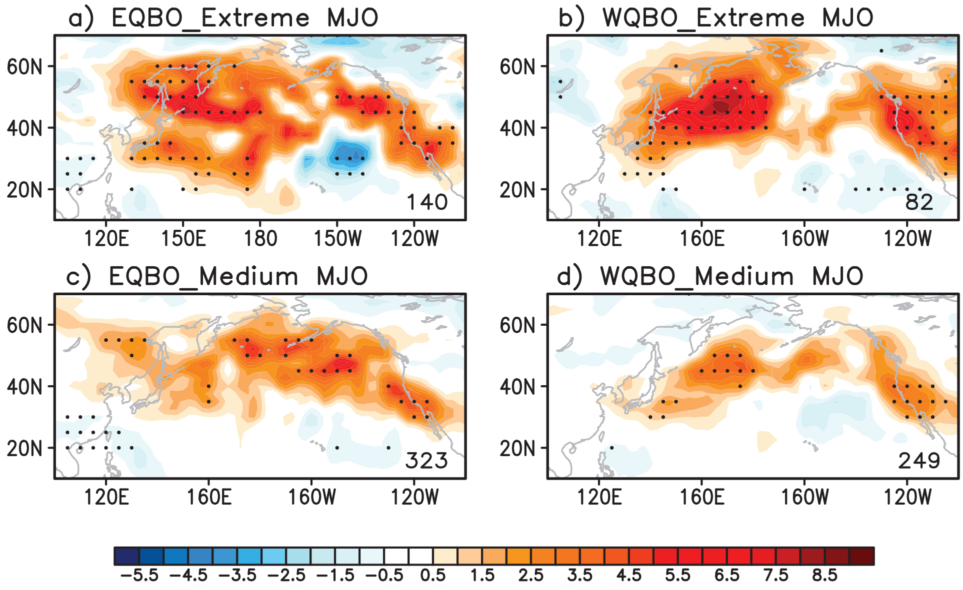

Figure 10. Composites of lagged 3- to 10-day EKE anomalies (m^2/s^2) during MJO phases 2–3 in (a and b) extreme strong MJO days (amplitude >2) and (c and d) medium strong MJO days (amplitude from 1 to 2) in (a and c) EQBO winters and (b and d) WQBO winters. The dotted areas represent significant EKE anomalies exceeding the 95% confidence level (plotted every 5°). Numbers of selected MJO days are indicated in the lower-right corner of each plot.

timescale, the NPST exhibits significant changes in response to the MJO. In general, when the MJO convection is located over the Indian Ocean (western to central Pacific), a poleward (southward) shift of the NPST is evident.

The intraseasonal variation of the northern flank of the NPST is significantly modulated by the QBO, which is summarized in Figure 11. The associated dynamical processes and the plausible contributors to the QBO-MJO-NPST relationship during MJO phases 2–3 (active convection over the Indian Ocean) are also illustrated. It is shown that both the amplitude and the spatial distribution of the MJO-related NPST change are modulated by the QBO. A more zonally elongated (separated) distribution of EKE anomalies with stronger (weaker) amplitude is observed in EQBO (WQBO) winters. The analysis of energy diagnostics indicates that the BCEC and EF dominate the NPST changes under the QBO modulation. Specifically, a monopole (dipole) energy source and a more continuous (disrupted) energy transport are found in EQBO (WQBO) winters, which may contribute to a uniform (separated) distribution of the NPST response to the MJO. The difference in the EKE amplitude is likely due to the different magnitude of the MJO-associated intraseasonal flow, which is caused by a change in the MJO divergence and RWS. On the other hand, the difference in the spatial distribution of the EKE anomalies may be a result of a direct impact of the QBO on the NPST. Similar conclusions can be implied for MJO phases 6–8.

This study mainly reveals a possible impact of different MJO amplitudes on the NPST under the QBO modulation. However, as pointed out by recent studies, the MJO not only has a lager amplitude but also exhibits a slower propagation in EQBO than WQBO winters (Marshall et al., 2017; Nishimoto & Yoden, 2017; Son et al., 2017). As demonstrated by Bladé and Hartmann (1995), with the increasing eastward phase speed of the tropical heating, the extratropical response diminishes in amplitude. They suggested that the reduced amplitude may be caused by a trapping of the excited Rossby wave within the easterly flow and a decrease in the Rossby wave group velocity. Their finding is confirmed by a recent study (Yadav & Straus, 2017). The MJO also propagates more continuously into the central Pacific in EQBO than WQBO winters (Marshall et al., 2017; Nishimoto & Yoden, 2017; Zhang & Zhang, 2018). According to Adames and Wallace (2014) and Bao and Hartmann (2014), the extratropical wave train is intensified when the MJO heating passes the Maritime Continent. They argued that this intensification arises from more efficient extraction of kinetic energy from the mean flow in the jet exit region. These results raise a possibility that the slower and more continuous MJO propagation in EQBO winters can induce a stronger extratropical circulation, and thereby influence the NPST.

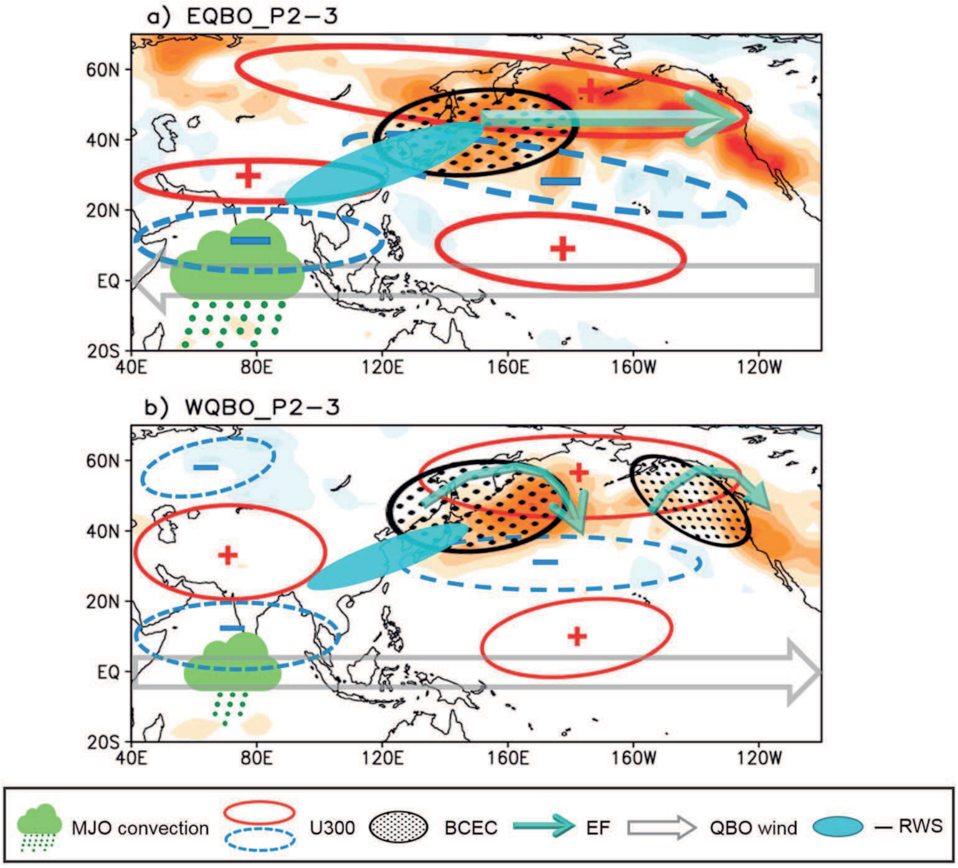

Figure 11. The schematic diagram of the MJO-NPST teleconnection during MJO phases 2–3 in (a) EQBO and (b) WQBO winters. U300, BCEC, EF (energy flux), and RWS are defined in the text. The shading represents EKE anomalies (m^2/s^2) shown in Figures 3c and 3e. All components, except the MJO convection, represent the 3- to 10-lagged-day averaged response to the MJO convection. The relative magnitude of the variables is indicated by the difference in the thickness, length, or size of the graph.

This study discusses the QBO impact on the MJO-NPST relationship in the lack of consideration of the ENSO impact. By examining the difference of intraseasonal NPST variance between the two ENSO phases, it is found that the NPST variance is significantly stronger during La Niña events than El Niño events over its southern flank (not shown). Therefore, ENSO also modulates the interannual change of intraseasonal NPST variation as suggested by Takahashi and Shirooka (2014). Given that EQBO winters are biased to La Niña phase (but no significant ENSO phase preference in WQBO winters) over the analysis period in this study (Figure S2 in Wang et al., 2018), a possible influence of ENSO on the MJO-NPST link in EQBO winters is tested. We discard EQBO winters that have significant La Niña events (3 discarded from 12 EQBO winters) and compare the results with our original results (Figures 3c and 3d). The spatial correlation coefficient of the NPST changes over 120°E–100°W, 20°–60°N between all EQBO winters and EQBO winters without La Niña winters is 0.82 for MJO phases 2–3 and 0.90 for MJO phases 6–8. Therefore, the inclusion of the ENSO effect in EQBO winters may not change the conclusion of this study. The negligible ENSO impact may be a result of different roles of ENSO and the QBO in the NPST variation: the QBO mainly influences the northern flank of the NPST, while ENSO primarily influences the southern flank (not shown). Further study is required to understand the mechanism and relative contributions of the QBO and ENSO to the NPST variation.

Although this study provides some insights into the possible mechanisms of the QBO-MJO-NPST relationship, the exact mechanism is still unclear and awaits confirmation by theoretical and modeling studies. One missing link stems from an unclear mechanism of the QBO-MJO connection. For example, most of previous studies have hypothesized that the QBO modulated static stability at the tropopause is the reason for stronger and continuous MJO during EQBO winters (Nishimoto & Yoden, 2017; Son et al., 2017). Zhang and Zhang

(2018), on the other hand, found that this hypothesis fails to explain why the MJO precipitation is weaker over the Indian Ocean but stronger over the western Pacific in EQBO than WQBO winters. In addition, studies have not reached to a consensus on what causes a stronger MJO activity in EQBO winters. Most of previous studies (Marshall et al., 2017; Nishimoto & Yoden, 2017; Son et al., 2017; Yoo & Son, 2016) attributed that to the greater amplitudes of individual MJO events, while Zhang and Zhang (2018) ascribed that to the larger number of MJO days. As such, the QBO-MJO connection is still unclear and a convincing mechanism for the QBO-MJO connection and its global impact warrant further study.

Acknowledgments
Constructive and valuable comments by Editor Chidong Zhang and three anonymous reviewers are greatly appreciated. The sources of data used in this study are as follows: https://www.esrl.noaa.gov/psd/mjo/mjoindex/ for the OMI, http://www.bom.gov.au/climate/mjo for the RMM index, http://apps.ecmwf.int/datasets/data/interim_full_daily for ERA-Interim reanalysis data, https://www.esrl.noaa.gov/psd/data/gridded/tables/daily.html for OLR daily data, and https://www.esrl.noaa.gov/psd/data/gridded/data.noaa.ersst.v4.html for Extended Reconstructed Sea Surface Temperature version 4. This research has been conducted as part of the NOAA MAPP S2S Prediction Task Force and supported by NOAA grant NA16OAR4310070 and NSF grant AGS-1652289. This study was also supported by the KMA Research and Development Program under grant KMI2018-03110 (Kim) and the Basic Science Research Program through the National Research Foundation funded by the Ministry of Science and ICT of Korea (2017R1E1A1A01074889; Son).

References

Adames, Á. F., & Wallace, J. M. (2014). Three-dimensional structure and evolution of the MJO and its relation to the mean flow. *Journal of the Atmospheric Sciences*, *71*(6), 2007–2026. https://doi.org/10.1175/JAS-D-13-0254.1

Alaka Jr, G. J., & Maloney, E. D. (2012). The influence of the MJO on upstream precursors to African easterly waves. *Journal of Climate*, *25*(9), 3219–3236. https://doi.org/10.1175/JCLI-D-11-00232.1

Athanasiadis, P. J., Wallace, J. M., & Wettstein, J. J. (2010). Patterns of wintertime jet stream variability and their relation to the storm tracks. *Journal of the Atmospheric Sciences*, *67*(5), 1361–1381. https://doi.org/10.1175/2009JAS3270.1

Baldwin, M., Gray, L., Dunkerton, T., Hamilton, K., Haynes, P., Randel, W., et al. (2001). The quasi-biennial oscillation. *Reviews of Geophysics*, *39*(2), 179–229. https://doi.org/10.1029/1999RG000073

Bao, M., & Hartmann, D. L. (2014). The response to MJO-like forcing in a nonlinear shallow-water model. *Geophysical Research Letters*, *41*, 1322–1328. https://doi.org/10.1002/2013GL057683

Blackmon, M. L. (1976). A climatological spectral study of the 500 mb geopotential height of the Northern Hemisphere. *Journal of the Atmospheric Sciences*, *33*(8), 1607–1623. https://doi.org/10.1175/1520-0469(1976)033%3C1607:ACSSOT%3E2.0.CO;2

Bladé, I., & Hartmann, D. L. (1995). The linear and nonlinear extratropical response of the atmosphere to tropical intraseasonal heating. *Journal of the Atmospheric Sciences*, *52*(24), 4448–4471. https://doi.org/10.1175/1520-0469(1995)052%3C4448:TLANER%3E2.0.CO;2

Brayshaw, D. J., Hoskins, B., & Blackburn, M. (2011). The basic ingredients of the North Atlantic storm track. Part II: Sea surface temperatures. *Journal of the Atmospheric Sciences*, *68*(8), 1784–1805. https://doi.org/10.1175/2011JAS3674.1

Cai, M., Yang, S., Van den Dool, H., & Kousky, V. (2007). Dynamical implications of the orientation of atmospheric eddies: A local energetics perspective. *Tellus A*, *59*(1), 127–140. https://doi.org/10.1111/j.1600-0870.2006.00213.x

Cassou, C. (2008). Intraseasonal interaction between the Madden–Julian oscillation and the North Atlantic oscillation. *Nature*, *455*(7212), 523–527. https://doi.org/10.1038/nature07286

Chang, E. K. M., Guo, Y., & Xia, X. (2012). CMIP5 multimodel ensemble projection of storm track change under global warming. *Journal of Geophysical Research*, *117*, D23118. https://doi.org/10.1029/2012JD018578

Chang, E. K. M., Lee, S., & Swanson, K. L. (2002). Storm track dynamics. *Journal of Climate*, *15*(16), 2163–2183. https://doi.org/10.1175/1520-0442(2002)015%3C02163:STD%3E2.0.CO;2

Chang, E. K. M., Ma, C. G., Zheng, C., & Yau, A. M. (2016). Observed and projected decrease in Northern Hemisphere extratropical cyclone activity in summer and its impacts on maximum temperature. *Geophysical Research Letters*, *43*, 2200–2208. https://doi.org/10.1002/2016GL068172

Chang, E. K. M., & Orlanski, I. (1994). On energy flux and group velocity of waves in baroclinic flows. *Journal of the Atmospheric Sciences*, *51*(24), 3823–3828. https://doi.org/10.1175/1520-0469(1994)051%3C3823:OEFAGV%3E2.0.CO;2

Chang, E. K. M., & Yau, A. M. (2016). Northern Hemisphere winter storm track trends since 1959 derived from multiple reanalysis datasets. *Clim. Dynam.*, *47*(5–6), 1435–1454. https://doi.org/10.1007/s00382-015-2911-8

Colle, B. A., Buonaiuto, F., Bowman, M. J., Wilson, R. E., Flood, R., Hunter, R., et al. (2008). New York City's vulnerability to coastal flooding: Storm surge modeling of past cyclones. *Bulletin of the American Meteorological Society*, *89*(6), 829–842. https://doi.org/10.1175/2007BAMS2401.1

Dee, D. P., Uppala, S., Simmons, A., Berrisford, P., Poli, P., Kobayashi, S., et al. (2011). The ERA-Interim reanalysis: Configuration and performance of the data assimilation system. *Quarterly Journal of the Royal Meteorological Society*, *137*(656), 553–597. https://doi.org/10.1002/qj.828

Deng, Y., & Jiang, T. (2011). Intraseasonal modulation of the North Pacific storm track by tropical convection in boreal winter. *Journal of Climate*, *24*(4), 1122–1137. https://doi.org/10.1175/2010JCLI3676.1

Dole, R. M., & Black, R. X. (1990). Life cycles of persistent anomalies. Part II: The development of persistent negative height anomalies over the North Pacific Ocean. *Monthly Weather Review*, *118*(4), 824–846. https://doi.org/10.1175/1520-0493(1990)118%0824:LCOPAP%2.0.CO;2

Duchon, C. E. (1979). Lanczos filtering in one and two dimensions. *Journal of Applied Meteorology*, *18*(8), 1016–1022. https://doi.org/10.1175/1520-0450(1979)018%3C1016:LFIOAT%3E2.0.CO;2

Eady, E. T. (1949). Long waves and cyclone waves. *Tellus*, *1*(3), 33–52.

Feldstein, S. B. (2002). Fundamental mechanisms of the growth and decay of the PNA teleconnection pattern. *Quarterly Journal of the Royal Meteorological Society*, *128*(581), 775–796. https://doi.org/10.1256/0035900021643683

Garfinkel, C. I., & Hartmann, D. L. (2011). The influence of the quasi-biennial oscillation on the troposphere in winter in a hierarchy of models. Part II: Perpetual winter WACCM runs. *Journal of the Atmospheric Sciences*, *68*(9), 2026–2041. https://doi.org/10.1175/2011JAS3702.1

Guo, Y., Shinoda, T., Lin, J., & Chang, E. K. (2017). Variations of northern hemisphere storm track and extratropical cyclone activity associated with the Madden-Julian Oscillation. *Journal of Climate*, *30*(13), 4799–4818. https://doi.org/10.1175/JCLI-D-16-0513.1

Harnik, N., & Chang, E. K. M. (2004). The effects of variations in jet width on the growth of baroclinic waves: Implications for midwinter Pacific storm track variability. *Journal of the Atmospheric Sciences*, *61*(1), 23–40. https://doi.org/10.1175/1520-0469(2004)061%3C0023:TEOVIJ%3E2.0.CO;2

Henderson, S. A., Maloney, E. D., & Barnes, E. A. (2016). The influence of the Madden–Julian oscillation on Northern Hemisphere winter blocking. *Journal of Climate*, *29*(12), 4597–4616. https://doi.org/10.1175/JCLI-D-15-0502.1

Henderson, S. A., Maloney, E. D., & Son, S.-W. (2017). Madden-Julian Oscillation Pacific teleconnections: The impact of the basic state and MJO representation in general circulation models. *Journal of Climate*, *30*(12), 4567–4587. https://doi.org/10.1175/JCLI-D-16-0789.1

Hendon, H. H., Wheeler, M. C., & Zhang, C. (2007). Seasonal dependence of the MJO–ENSO relationship. *Journal of Climate*, *20*(3), 531–543. https://doi.org/10.1175/JCLI4003.1

Horel, J. D., & Wallace, J. M. (1981). Planetary-scale atmospheric phenomena associated with the Southern Oscillation. *Monthly Weather Review*, *109*(4), 813–829. https://doi.org/10.1175/1520-0493(1981)109%3C0813:PSAPAW%3E2.0.CO;2

Hoskins, B. J., James, I. N., & White, G. H. (1983). The shape, propagation and mean-flow interaction of large-scale weather systems. *Journal of the Atmospheric Sciences*, *40*(7), 1595–1612. https://doi.org/10.1175/1520-0469(1983)040%3C1595:TSPAMF%3E2.0.CO;2

Hoskins, B. J., & Karoly, D. J. (1981). The steady linear response of a spherical atmosphere to thermal and orographic forcing. *Journal of the Atmospheric Sciences*, *38*(6), 1179–1196. https://doi.org/10.1175/1520-0469(1981)038%3C1179:TSLROA%3E2.0.CO;2

Hsu, H.-H. (1996). Global view of the intraseasonal oscillation during northern winter. *Journal of Climate*, *9*(10), 2386–2406. https://doi.org/10.1175/1520-0442(1996)009%3C2386:GVOTIO%3E2.0.CO;2

Huang, B., Banzon, V. F., Freeman, E., Lawrimore, J., Liu, W., Peterson, T. C., et al. (2015). Extended reconstructed sea surface temperature version 4 (ERSST. v4). Part I: Upgrades and intercomparisons. *Journal of Climate*, *28*(3), 911–930. https://doi.org/10.1175/JCLI-D-14-00006.1

Kiladis, G. N., Dias, J., Straub, K. H., Wheeler, M. C., Tulich, S. N., Kikuchi, K., et al. (2014). A comparison of OLR and circulation-based indices for tracking the MJO. *Monthly Weather Review*, *142*(5), 1697–1715. https://doi.org/10.1175/MWR-D-13-00301.1

Kunkel, K. E., Easterling, D. R., Kristovich, D. A., Gleason, B., Stoecker, L., & Smith, R. (2012). Meteorological causes of the secular variations in observed extreme precipitation events for the conterminous United States. *Journal of Hydrometeorology*, *13*(3), 1131–1141. https://doi.org/10.1175/JHM-D-11-0108.1

Lau, W. K. M., & Waliser, D. E. (2011). *Intraseasonal Variability of the Atmosphere–Ocean Climate System, 2nd ed* (p. 613). Germany: Springer, Heidelberg.

Lee, S.-S., Lee, J.-Y., Wang, B., Ha, K.-J., Heo, K.-Y., Jin, F.-F., et al. (2012). Interdecadal changes in the storm track activity over the North Pacific and North Atlantic. *Climate Dynamics*, *39*(1–2), 313–327. https://doi.org/10.1007/s00382-011-1188-9

Lee, Y. Y., & Lim, G. H. (2012). Dependency of the North Pacific winter storm tracks on the zonal distribution of MJO convection. *Journal of Geophysical Research*, *117*, D14101. https://doi.org/10.1029/2011JD016417

Li, Y. (2011). *Dynamical Mechanisms for the Teleconnection between ENSO and NAO in Late Winter* (Doctoral dissertation). Princeton University.

Lin, H., Brunet, G., & Derome, J. (2009). An observed connection between the North Atlantic Oscillation and the Madden–Julian oscillation. *Journal of Climate*, *22*(2), 364–380. https://doi.org/10.1175/2008JCLI2515.1

Linkin, M. E., & Nigam, S. (2008). The North Pacific Oscillation–west Pacific teleconnection pattern: Mature-phase structure and winter impacts. *Journal of Climate*, *21*(9), 1979–1997. https://doi.org/10.1175/2007JCLI2048.1

Madden, R. A., & Julian, P. R. (1971). Detection of a 40–50 day oscillation in the zonal wind in the tropical Pacific. *Journal of the Atmospheric Sciences*, *28*(5), 702–708. https://doi.org/10.1175/1520-0469(1971)028%3C0702:DOADOI%3E2.0.CO;2

Madden, R. A., & Julian, P. R. (1972). Description of global-scale circulation cells in the tropics with a 40–50 day period. *Journal of the Atmospheric Sciences*, *29*(6), 1109–1123. https://doi.org/10.1175/1520-0469(1972)029%3C1109:DOGSCC%3E2.0.CO;2

Madden, R. A., & Julian, P. R. (1994). Observations of the 40–50-day tropical oscillation—A review. *Monthly Weather Review*, *122*(5), 814–837. https://doi.org/10.1175/1520-0493(1994)122%3C0814:OOTDTO%3E2.0.CO;2

Marshall, A. G., Hendon, H. H., Son, S.-W., & Lim, Y. (2017). Impact of the quasi-biennial oscillation on predictability of the Madden–Julian oscillation. *Climate Dynamics*, *49*(4), 1365–1377. https://doi.org/10.1007/s00382-016-3392-0

Moon, J.-Y., Wang, B., & Ha, K.-J. (2011). ENSO regulation of MJO teleconnection. *Climate Dynamics*, *37*(5–6), 1133–1149. https://doi.org/10.1007/s00382-010-0902-3

Mori, M., & Watanabe, M. (2008). The growth and triggering mechanisms of the PNA: A MJO-PNA coherence. *Journal of the Meteorological Society of Japan*, *86*(1), 213–236. https://doi.org/10.2151/jmsj.86.213

Mundhenk, B. D., Barnes, E. A., & Maloney, E. D. (2016). All-season climatology and variability of atmospheric river frequencies over the North Pacific. *Journal of Climate*, *29*(13), 4885–4903. https://doi.org/10.1175/JCLI-D-15-0655.1

Nakazawa, T. (2000). MJO and tropical cyclone activity during 1997/98 ENSO. *Advances in Space Research*, *25*(5), 953–958. https://doi.org/10.1016/S0273-1177(99)00928-X

Nishimoto, E., & Yoden, S. (2017). Influence of the stratospheric quasi-biennial oscillation on the Madden–Julian Oscillation during austral summer. *Journal of the Atmospheric Sciences*, *74*(4), 1105–1125. https://doi.org/10.1175/JAS-D-16-0205.1

Orlanski, I., & Sheldon, J. (1993). A case of downstream baroclinic development over western North America. *Monthly Weather Review*, *121*(11), 2929–2950. https://doi.org/10.1175/1520-0493(1993)121%2929:ACODBD%2.0.CO;2

Pohl, B., & Matthews, A. J. (2007). Observed changes in the lifetime and amplitude of the Madden–Julian oscillation associated with interannual ENSO sea surface temperature anomalies. *Journal of Climate*, *20*(11), 2659–2674. https://doi.org/10.1175/JCLI4230.1

Salathé, E. P. (2006). Influences of a shift in North Pacific storm tracks on western North American precipitation under global warming. *Geophysical Research Letters*, *33*, L19820. https://doi.org/10.1029/2006GL026882

Sardeshmukh, P. D., & Hoskins, B. J. (1988). The generation of global rotational flow by steady idealized tropical divergence. *Journal of the Atmospheric Sciences*, *45*(7), 1228–1251. https://doi.org/10.1175/1520-0469(1988)045%3C1228:TGOGRF%3E2.0.CO;2

Seo, J., Choi, W., Youn, D., Park, D. S. R., & Kim, J. Y. (2013). Relationship between the stratospheric quasi-biennial oscillation and the spring rainfall in the western North Pacific. *Geophysical Research Letters*, *40*, 5949–5953. https://doi.org/10.1002/2013GL058266

Seo, K.-H., & Lee, H.-J. (2017). Mechanisms for a PNA-like teleconnection pattern in response to the MJO. *Journal of the Atmospheric Sciences*, *74*(6), 1767–1781. https://doi.org/10.1175/JAS-D-16-0343.1

Simmons, A., Wallace, J., & Branstator, G. (1983). Barotropic wave propagation and instability, and atmospheric teleconnection patterns. *Journal of the Atmospheric Sciences*, *40*(6), 1363–1392. https://doi.org/10.1175/1520-0469(1983)040%3C1363:BWPAIA%3E2.0.CO;2

Simmons, A. J., & Hoskins, B. J. (1978). The life cycles of some nonlinear baroclinic waves. *Journal of the Atmospheric Sciences*, *35*(3), 414–432. https://doi.org/10.1175/1520-0469(1978)035%3C0414:TLCOSN%3E2.0.CO;2

Son, S.-W., Lim, Y., Yoo, C., Hendon, H. H., & Kim, J. (2017). Stratospheric control of the Madden–Julian Oscillation. *Journal of Climate*, *30*(6), 1909–1922. https://doi.org/10.1175/JCLI-D-16-0620.1

Son, S.-W., Ting, M., & Polvani, L. M. (2009). The effect of topography on storm-track intensity in a relatively simple general circulation model. *Journal of the Atmospheric Sciences*, *66*(2), 393–411. https://doi.org/10.1175/2008JAS2742.1

Stan, C., Straus, D. M., Frederiksen, J. S., Lin, H., Maloney, E. D., & Schumacher, C. (2017). Review of tropical-extratropical teleconnections on intraseasonal time scales. *Reviews of Geophysics*, *55*, 902–937. https://doi.org/10.1002/2016RG000538

Takahashi, C., & Shirooka, R. (2014). Storm track activity over the North Pacific associated with the Madden-Julian Oscillation under ENSO conditions during boreal winter. *Journal of Geophysical Research: Atmospheres*, *119*, 10,663–10,683. https://doi.org/10.1002/2014JD021973

Taylor, K. E. (2001). Summarizing multiple aspects of model performance in a single diagram. *Journal of Geophysical Research*, *106*(D7), 7183–7192. https://doi.org/10.1029/2000JD900719

Wallace, J. M., & Gutzler, D. S. (1981). Teleconnections in the geopotential height field during the Northern Hemisphere winter. *Monthly Weather Review*, *109*(4), 784–812. https://doi.org/10.1175/1520-0493(1981)109%3C0784:TITGHF%3E2.0.CO;2

Wallace, J. M., Lim, G.-H., & Blackmon, M. L. (1988). Relationship between cyclone tracks, anticyclone tracks and baroclinic waveguides. *Journal of the Atmospheric Sciences*, *45*(3), 439–462. https://doi.org/10.1175/1520-0469(1988)045%3C0439:RBCTAT%3E2.0.CO;2

Wang, J., Kim, H.-M., & Chang, E. K. M. (2018). Interannual modulation of northern hemisphere winter storm tracks by the QBO. *Geophysical Research Letters*, *45*. https://doi.org/10.1002/2017GL076929

Wang, J., Wen, Z., Wu, R., Guo, Y., & Chen, Z. (2016). The mechanism of growth of the low-frequency East Asia-Pacific teleconnection and the triggering role of tropical intraseasonal oscillation. *Climate Dynamics*, *46*(11-12), 3965–3977. https://doi.org/10.1007/s00382-015-2815-7

Wheeler, M. C., & Hendon, H. H. (2004). An all-season real-time multivariate MJO index: Development of an index for monitoring and prediction. *Monthly Weather Review*, *132*(8), 1917–1932. https://doi.org/10.1175/1520-0493(2004)132%3C1917:AARMMI%3E2.0.CO;2

Woollings, T., Gregory, J. M., Pinto, J. G., Reyers, M., & Brayshaw, D. J. (2012). Response of the North Atlantic storm track to climate change shaped by ocean-atmosphere coupling. *Nature Geoscience*, *5*(5), 313–317. https://doi.org/10.1038/ngeo1438

Yadav, P., & Straus, D. M. (2017). Circulation response to fast and slow MJO episodes. *Monthly Weather Review*, *145*(5), 1577–1596. https://doi.org/10.1175/MWR-D-16-0352.1

Yoo, C., & Son, S. W. (2016). Modulation of the boreal wintertime Madden-Julian Oscillation by the stratospheric quasi-biennial oscillation. *Geophysical Research Letters*, *43*, 1392–1398. https://doi.org/10.1002/2016GL067762

Zhang, C. (2005). Madden-Julian Oscillation. *Reviews of Geophysics*, *43*, RG2003. https://doi.org/10.1029/2004RG000158

Zhang, C., Gottschalck, J., Maloney, E. D., Moncrieff, M., Vitart, F., Waliser, D. E., et al. (2013). Cracking the MJO nut. *Geophysical Research Letters*, *40*, 1223–1230. https://doi.org/10.1002/grl.50244

Zhang, C., & Zhang, B. (2018). QBO-MJO connection. *Journal of Geophysical Research*, *123*. https://doi.org/10.1002/2017JD028171